Gradually Fe-doped Co_3O_4 nanoparticles in 2-propanol and water oxidation catalysis with single laser pulse resolution.

Swen Zerebecki [1,2], Kai Schott[1,2], Soma Salamon[1,3], Joachim Landers[1,3] Heiko Wende[1,3], Eko Budiyanto[4], Harun Tüysüz[4], Stephan Barcikowski[1,2], Sven Reichenberger*[1,2]

[1]Center for Nanointegration Duisburg-Essen (CENIDE), University of Duisburg-Essen, 47057 Duisburg, Germany

[2]Technical Chemistry I, University of Duisburg-Essen, 45141 Essen, Germany

[3]Faculty of Physics, University of Duisburg-Essen, Lotharstr. 1, 47057 Duisburg, Germany

[4]Max-Planck-Institut für Kohlenforschung, Kaiser-Wilhelm-Platz 1, 45470 Mülheim an der Ruhr, Germany

*corresponding author

Keywords: reactive laser processing, pulsed laser processing in liquid, inverse spinel, oxidation catalysis, defects, colloids, free liquid jet

Abstract

Controlling the surface composition of colloidal nanoparticles is still a challenging yet mandatory prerequisite in catalytic studies to investigate composition-activity trends, active sites, and reaction mechanisms without superposition of particle size- or morphology-effects. Laser post-processing of colloidal nanoparticles has been employed previously to create defects in oxide nanoparticles, while the possibility of laser-based cation doping of colloidal nanoparticles without affecting their size, remains mostly unaccounted for. Consequently, at the example of doping iron into colloidal Co_3O_4 spinel nanoparticles, we developed a pulse-by-pulse laser cation doping method to provide catalyst series with gradual surface composition but maintained extrinsic properties such as phase, size, and surface area for catalytic studies. Laser pulse number-resolved doping series were prepared at laser intensity chosen to selectively heat the Co_3O_4-NPs to roughly 1000 K and enable cation diffusion of surface-adsorbed Fe^{3+} into the Co_3O_4 lattice while maintaining the spinel phase, particle size, and surface area. The combination of bulk-sensitive X-ray fluorescence (XRF) and

surface-sensitive X-ray photoelectron spectroscopy (XPS) was used to confirm a surface enrichment of the Fe-dopant. XRD, Magnetometry, and Mössbauer spectroscopy revealed an increasing interaction between Fe and the antiferromagnetic Co_3O_4 with an increasing number of pulses, in line with a proposed laser-induced surface doping of colloidal Co_3O_4 with Fe. Using Fick's second law the thermal diffusion-related doping depth was estimated to be roughly 2 nm after 4 laser pulses. At the example of gas-phase 2-propanol oxidation and liquid-phase oxygen evolution reaction, the activity of the laser-doped catalysts is in good agreement with previous observations on binary iron-cobalt oxides. The catalytic activity was found to linearly increases with the calculated doping depth in both reactions, while only catalysts processed with at least one laser pulse were catalytically stable, highlighting the presented method in providing comparable, active, and stable gradual catalyst doping series for future catalytic studies.

Graphical Abstract:

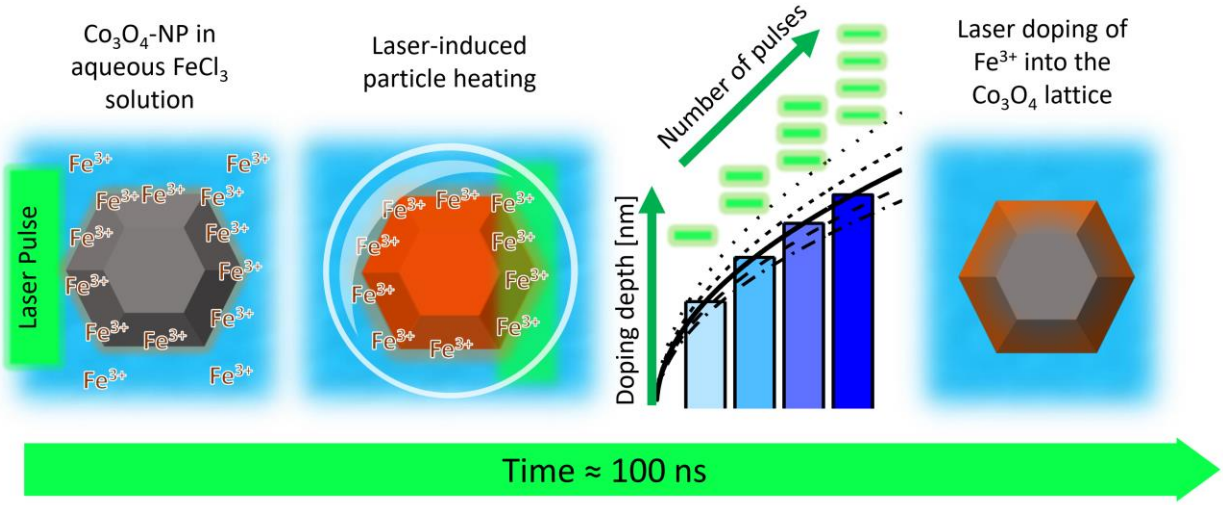

1 Introduction

Metal oxides are important catalysts in various industrial applications.[1] Yet, rarely pure oxides are used in large-scale application, since the introduction of a small fraction of cations or anions to host oxides typically improves their activity or selectivity. Parravano first intentionally synthesized doped oxides in 1953.[2] However, McFarland and Metiu also highlighted that most deployed oxide catalysts potentially contain low amounts of impurities or additives which might unknowingly

contribute to the performance of the catalyst[3] rendering the identification of the active sites in heterogeneous oxide catalysts very challenging.

Co_3O_4 is a very promising oxidation catalyst for gas phase, liquid phase, and electrocatalysis, which however still only finds limited industrial use due to selectivity and stability limitations. Recent catalytic studies with pure and partially iron-substituted Co_3O_4 have shown that the catalyst performance and stability[4,5] is significantly influenced by the Fe:Co ratio[5–7], the size[8–11], and the shape of Co_3O_4[10,12] as well as $CoFe_2O_4$[5,13] particles. In the case of the gas-phase oxidation of 2-propanol over Co_3O_4, it was proposed that surface-near five-fold-coordinated octahedral Co_{5c}^{3+} acts as an active site for the oxidation to acetone[14]. Substitution of Co_3O_4 with small amounts of Fe^{3+} (<10 at%) was shown to cause a decrease in activity in both the gas- and the liquid-phase oxidation of 2-propanol to acetone and acetic acid, respectively since undercoordinated octahedral Co^{3+} sites are replaced by Fe^{3+}.[7] On the contrary the electrocatalytic oxygen evolution reaction (OER) activity of iron-containing Co_3O_4 was found to slightly improve in the presence of small at% of iron.[5] The tetrahedral Co^{2+} cations were discussed as key active sites for the formation of μ-OOH species during the OER reaction.[5] However, higher iron contents (>13 at%; Co:Fe ratio of 7) turned out to be increasingly detrimental causing a gradually decreasing OER activity which succumbs to the activity of pure Co_3O_4 when exceeding ~25at% iron (Co:Fe ratio of 3).[5] Additionally, at 5 at% of Fe-doping, an activity maximum was found for the oxidation of styrene, benzyl alcohol, and cinnamyl alcohol with *tert*-butyl hydroperoxide (TBHP) as an oxidizing agent while the activity steadily decreased over the whole iron-doping concentration when oxygen was used as the oxidizing agent.[6] The observed activity trends were discussed to highlight different activation mechanisms such as the decomposition of the peroxide to form reactive oxygen radicals and a spin transfer to activate the oxygen, providing new hints to identify the active site and related reaction mechanisms occurring for each oxidizing agent in future studies.[6]

In conventional synthesis methods used for the synthesis of the previously discussed oxide catalysts (as in the previous studies) the dopant or substituting cation (e.g. iron in Co_3O_4) is typically added during the particle synthesis to achieve bulk substitution yet potentially also affecting the particle growth (a final size) demanding careful optimization of the synthesis protocol to maintain particle size, BET surface area, and surface termination throughout the dopant series.[15] In 2D-film synthesis on the other hand, either bulk-substituted thin-film composition libraries are

gained by magnetron sputtering,[16] or surface-near cation substitution is achieved by post-synthesis treatment e.g. by ion-implantation,[17] in-diffusion (from solids or gases),[18] and laser-induced doping.[19] Yet, challenges like self-purification, particularly in the case of non-thermodynamically favored dopant induction,[20] demand for a limitation of the long-term heat load in order to kinetically stabilize the dopants in the lattice by fast temperature quenching.

Pulsed lasers provide an ideal tool to fulfill the previously mentioned requirements. At the example of gas-phase doping of wafers with pulsed lasers, two doping mechanisms were discussed in the past. On the one hand, in the case of p- and n-doping of Si-wafers with pulsed lasers a thermally-induced atom diffusion occurring throughout the nanosecond excitation (heating) of the laser-excited Si wafers was discussed[21] while for laser doping of gaseous chromium precursors into SiC wafers a laser-induced thermal stress-mediated mechanism was proposed.[22] When turning towards colloidal nanoparticles instead of wafers as well as liquids instead of gas-phase processing only H-doping of NiO on post-irradiation of colloidal NiO in ethanol with pulsed lasers has been reported in the past.[23] Yet, laser-induced cation doping of colloidal nanoparticles by pulsed laser post-processing (PLPP) with single laser pulses and the correlation of surface doping and catalytic activity is still an open field. Hereby, PLPP holds particular opportunities since PLPP has been reported to kinetically stabilize catalysis-relevant metastable structures such as amorphous,[24,25] defective[19], and/or single-atom catalysts[26] while maintaining the particle size and oxide phase when choosing a sufficient laser intensity regime.[27,28]

In this study, we investigated a heat-induced, diffusion-controlled pulse-by-pulse laser-doping strategy of spinel-based Co_3O_4 catalyst particles with iron cations to systematically correlate the laser-imprinted dopant surface-concentration with the catalytic activity (or selectivity). Laser-doping of the colloidal nanoparticles was conducted using a previously developed continuously operating flat liquid jet setup.[28] The continuous flow ensures the illumination of each colloid volume element by a single laser pulse during one passage through the setup.[28] Multiple passages allow for a gradual pulse-by-pulse processing[27,29] and hence a laser pulse-resolved doping of the colloid as well as the correlation of the doping process and the catalytic activity. The flat liquid jet geometry of the setup ensures uniform illumination conditions (laser fluence) which were found mandatory to maintain the initial particle properties such as size, crystal phase, and BET-area (at adequately low laser intensity).[27,29] On solving 2nd Fick's equation considering relevant

temperatures and heating times of pulsed laser heating it will be shown that the developed laser-induced surface doping method for nanoparticles, allows the control of the doping depth by the variation of the number of applied pulses. XRD measurements reveal an increase of the Co_3O_4 lattice parameter with the rising number of step-by-step applied laser pulses indicating the incorporation of Fe into the Co_3O_4 lattice. HR-TEM/EDX shows the homogeneous distribution of the dopant. Utilizing XPS as surface-sensitive and XRF as bulk-sensitive method the dopant enrichment at the surface was confirmed. The diffusion of surface Fe into the Co_3O_4 was tracked with magnetometry and Mössbauer spectroscopy measurements while using ^{57}Fe isotope as the dopant. The doped catalysts were tested in the 2-propanol oxidation and the electrochemical OER revealing an increase in activity after the laser treatment in correlation with the doping depth.

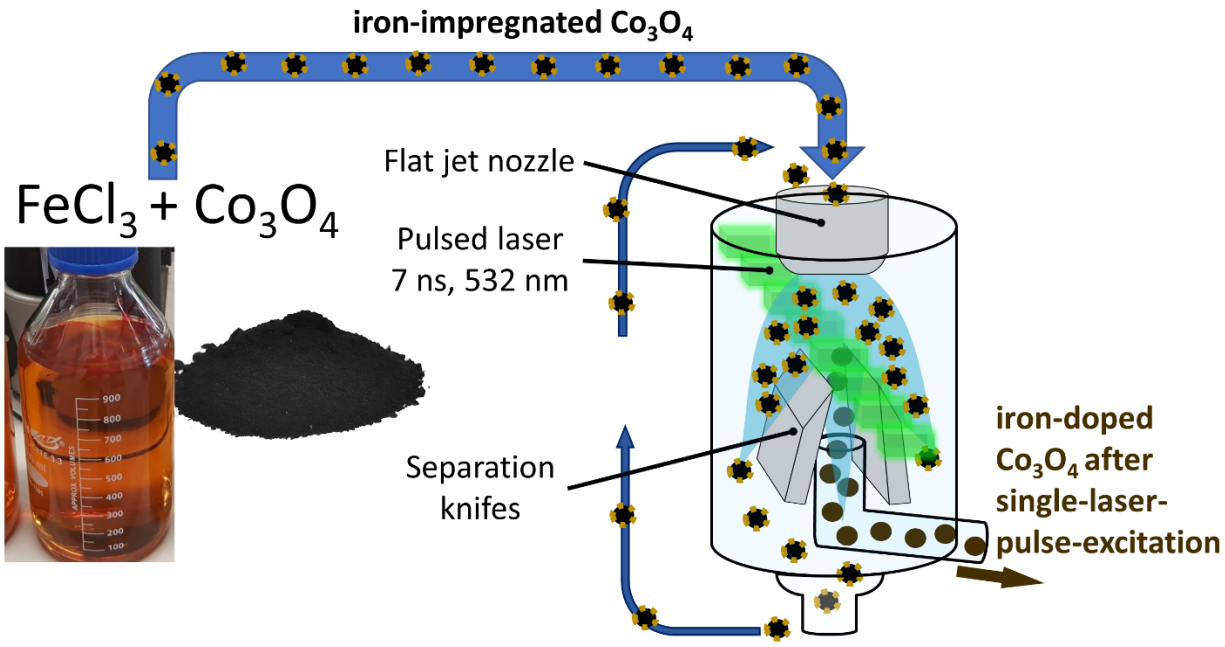

Figure 1: Scheme on the performed laser-doping of Co3O4 with Fe3+ cations under single pulse per particle conditions.

2 Experimental details

300 mg Co_3O_4-powder (<50 nm, Merck 637025) were ground, then dispersed in 1 L of MilliQ water containing 0.5 mmol/L and 2 mmol/L of $FeCl_3$, and finally sonicated for 60 min using an ultrasonication bath. The pH value of the dispersion was kept at around 2.7-3.3 to ensure that the Fe^{3+} stays dissolved as Fe^{3+}, $Fe(OH)^{2+}$ and $Fe(OH)_2^{+}$ while avoiding potential precipitation as $Fe(OH)_3$ which would occur above pH 5.[30]

PLPP: To initiate Fe-doping of the Co_3O_4-particles, the as-prepared dispersion was irradiated by a 532 nm pulsed laser (IS400-1-L, SHG, Edgewave) with a pulse duration of ~7 ns, 5 kHz repetition rate, at a spot size of 0.3709 mm², see Fig S1. The pulsed laser post-processing (PLPP) was performed in a continuous-flow flat jet setup, to enable uniform irradiation under one pulse per volume element conditions.[28] After the treatment, particles and liquid phase were separated by centrifugation at 15000 rpm for 60 min. The resulting pellet was dispersed in MilliQ -water 3 times and centrifuged to remove any excess Fe- and Cl-ions to be subsequently freeze-dried.

In order to obtain Mössbauer spectra with sufficient resolution even at very low overall Fe-content, the pulse-by-pulse-resolved laser-doping series prepared with the 0.5 mmol/L $FeCl_3$ precursor solution was conducted using pure ^{57}Fe isotope (enriched to >95%, Chemotrade GmbH). This strongly increases the fraction of resonant nuclear absorption, while not altering the chemical properties of the resulting particles. The $^{57}FeCl_3$ solution was prepared by dissolving metallic ^{57}Fe in 30% HCl and 30% H_2O_2. The dissolved $^{57}Fe^{3+}$ was then precipitated with NaOH as $^{57}Fe(OH)_3$ and washed with MilliQ-Water 3 times by centrifugation. The $^{57}Fe(OH)_3$ was dissolved in a pH 3 HCl solution and utilized for Fe-doping of Co_3O_4 particles in the same manner as described for the previously specified $FeCl_3$ solution.

Material characterization:

High-resolution TEM (HRTEM) and energy-dispersive X-ray spectroscopy (EDX) was performed with a JEOL JEM 2200FS equipped with a chemiSTEM EDX detector system.

X-ray photoelectron spectroscopy (XPS) measurements were carried out with a PHI 5000 Versaprobe II, utilizing a monochromatic aluminum anode with a K_α line at 1486.6 eV, a spot size of 100 μm, a hemispherical analyzer (with an angle of 45° between the surface of the sample and the analyzer), and dual beam charge neutralization. All XPS spectra were referenced to the C 1s signal of hydrocarbons (284.8 eV) found in every corresponding sample. Baseline correction (Shirley) and fitting of the corrected XPS signals were conducted with Casa XPS.

X-ray diffraction (XRD) measurements were conducted on a D8 ADVANCE (Bruker) powder diffractometer with Cu-Kα radiation (λ = 0.15418 nm, 40 Kv, and 40 Ma). The cell parameter and the size of the coherent diffraction domain were determined with MAUD software which is based on the Rietveld method combined with Fourier analysis, well adapted for broadened diffraction peaks. LaB_6 was used as a standard to quantify the instrumental broadening contribution.

Mössbauer spectra were recorded in transmission geometry on powder samples, using a ^{57}Co(Rh) radiation source mounted on a constant acceleration driving unit. Low temperatures and high magnetic fields were achieved using a liquid helium bath cryostat, containing a superconducting solenoid in split-pair geometry, allowing measurements to be performed at 4.3 K under a magnetic field of 5 T applied parallel to the γ-ray propagation direction. Additional reference spectra were recorded between 5 K and 300 K using a closed-cycle cryostat (Lake Shore Cryotronics). All spectra were evaluated using the "Pi"-program package.[31]

Electrochemical oxygen evolution reaction (OER) measurements were performed with BioLogic VSP-300 Potentiostat coupled with a rotating disc electrode (Model: AFMSRCE, PINE Research Instrumentation) using a three-electrodes system. Pt wire was used as the counter electrode and a hydrogen reference electrode (HydroFlex, Gaskatel) as the reference electrode. The measurement was done in alkaline conditions using 1 M KOH as the electrolyte. The working electrodes were prepared by depositing electrocatalyst ink onto glassy carbon (GC) electrodes (5 mm diameter, 0.196 cm^2 geometric surface area, PINE Research Instrumentation). Before the catalyst deposition, GC electrodes were polished with Alumina micropolish suspension (1 and 0. 5 μm, Buehler). To prepare ink, 4.8 mg of electrocatalyst powder was dispersed in 0.75 mL of Mili-Q water (18.2 MΩ.cm) and 0.25 mL isopropanol. 50 μL Nafion 117 (Sigma Aldrich) was then added to the dispersion as the binding agent followed by sonication for 30 minutes to get a homogeneous ink. Finally, 5.25 μL of the ink was drop-casted onto a clean GC electrode surface and dried under lamp radiation and Ar flow (calculated catalyst loading was equal to 0.12 mg/cm^2). Linear scan voltammetry (LSV) curve was measured in the scan rate of 10 mV/s within the potential bias of 0.7 V to 1.7 V vs RHE and 2000 rpm working electrode rotation speed. Cyclic voltammetry (CV) was recorded in the scan rate of 50 mV/s within the potential bias of 0.7 V to 1.6 V vs RHE. The IR drop was compensated at 85% for all measurements.

3 Results and Discussion

HR-TEM/EDX analyses of the dry Co_3O_4 particles after the dispersion in a 2 mmol/L $FeCl_3$ and 3 times washing with Milli-Q water are displayed in Fig. 2 a-d. The HR-TEM showed that small clusters have formed on top of the Co_3O_4 crystals (see Fig. 2 a, b). In the case of samples impregnated with 0.5 mmol/L dopant solutions did not indicate the formation of these clusters

(compare Fig. S2). EDX investigation of the high dopant concentration impregnation (2 mmol/L $FeCl_3$) shows green-colored particle edges in Fig. 2 c. A quantification suggests the presence of ~21 at% of adsorbed iron precursor on the surface after the impregnation and washing steps. Consequently, the clusters observed in HR-TEM after Fe^{3+} impregnation likely resemble FeO(OH) clusters that formed from the adsorbed ions[32,33] when the samples were dried during TEM grid preparation. The former is confirmed in the EDX-line scan (Fig. 2 d) where indications of Fe can be only found outside of the Co_3O_4. Although none of the clusters were observed in the case of samples impregnated by the low dopant concentration of 0.5 mmol/L, still 5-6 at% of Fe was found after impregnation and washing (compare Fig. S2 c).

Pulse-by-Pulse laser doping of the colloidal Co_3O_4 sample with Fe^{3+} cations was conducted in several subsequent passages of the colloidal Co_3O_4 dispersion through a self-developed flat liquid jet setup (previously introduced[28], successfully employed[27,29], and depicted in Fig. 1). The setup enables to apply an individual laser pulse with uniform laser intensity to each volume element (containing the iron-impregnated colloidal Co_3O_4 nanoparticles) that passages through the illuminated cross-section.[28] Gradual laser pulse-resolved Co_3O_4 doping series with Fe^{3+} after application of 1, 2, 3, and 4 individual processing steps resembling a pulse-by-pulse laser treatment were prepared for two precursor concentrations (0.5 mmol/L $^{57}FeCl_3$ and 2 mmol/L $FeCl_3$, respectively) by passing the colloid through the setup in 1-4 passages. For the high precursor concentration of 2 mmol/L, respective HR-TEM and EDX investigations after pulse-by-pulse laser treatment with 1 and 4 laser pulses are shown in Fig. 2 e-h and Fig. 2 i-l. As can be seen, after pulse-by-pulse processing of Co_3O_4 with a single or multiple subsequent laser pulses, the FeO(OH)-clusters disappeared. Yet, EDX mapping of laser-doped samples (Fig. 2 g and k) indicate that iron still is located in the surface-near regions of the Co_3O_4 sample. However, the Fe signals appear to have weakened or spatially broadened upon laser treatment, particularly visible within the EDX line scans (Fig. 2 h and l), which renders the determination of the Fe-dopant location from EXD investigation rather difficult. Additionally, after later treatment, a disordered surface layer seems to be recognizable in the HR-TEM pictures in Fig. 2 f, j and Fig S2 f, j, which was also previously observed for laser-treated $CoFe_2O_4$ and assigned to the presence of surface hydroxides[29].

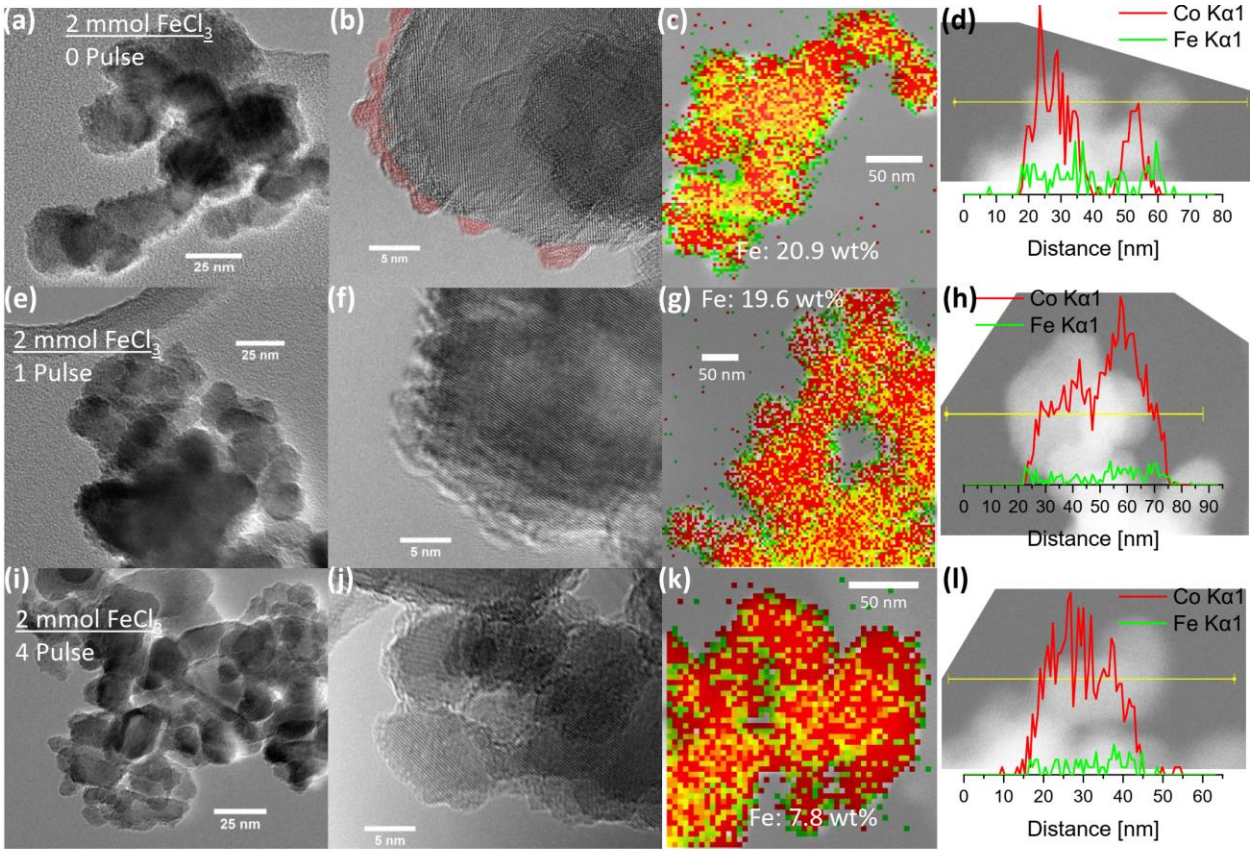

Figure 2:HR-TEM/EDX of Co_3O_4 after dispersion and separation from a 2 mmol $FeCl_3$ solution. (a)-(d) without laser treatment. (e)-(h) with 1 pulse and (i)-(l) with 3 applied pulses.

To discriminate the presence of Fe in the surface and within the overall sample, both, XPS and XRF analysis was conducted, respectively. Hereby, XPS can be considered as a surface-sensitive method. In the case of an epitaxial grown Co_3O_4 film, comparable excitation angle of 45° used here, and the given x-ray source intensity, Vaz et al. determined the information depth to be 1-2 nm[34] representing the well-known high surface sensitivity of XPS. Yet, to avoid later misconceptions it stands to be noted that XPS does not represent the composition of the first surface layer alone, but resembles an average composition over several surface layers. Contrarily, the information depth of XRF is in the range of more than 1 µm which significantly exceeds the particle diameter of <50 nm rendering XRF sensitive to the overall particle composition[35].

The analysis results for both gradual laser pulse-resolved Co_3O_4 doping series impregnated at iron precursor concentrations of 0.5 mmol/L and 2 mmol/L, respectively are summarized in Fig. 3 a. Considering all investigated samples the at% of iron determined from the Fe 3p and Co 3p XPS signal (see Fig. S4) was found to be 2-6 times higher than the iron content found with XRF

indicating a high concentration of iron in the first surface layers of the laser-processed Co_3O_4 particles. Interestingly, in the case of the sample series prepared with 0.5 mmol/L $FeCl_3$, the Fe content slightly increases after the first laser pulse was employed while for 2 mmol/L $FeCl_3$ the Fe content strongly declines, respectively. This observation may point towards a partial laser-induced dissolution / desorption of the iron precursor adsorbed on the Co_3O_4 surface after impregnation in case of the high precursor concentration. To elucidate the interpretation of a potential laser-induced dissolution / desorption t higher concentration of $FeCl_3$, a concentration series was prepared and investigated by XRF (shown in Fig. S3) before and after employing the first laser pulse. In case of an $FeCl_3$-concentrations between 0.01-0.5 mmol/L (and subsequent 3x washing in MilliQ water) the Fe content on the Co_3O_4 stays relatively constant at 2-3 wt% independent whether a single laser pulse was employed or not, while for 1 and 2 mmol/L $FeCl_3$ the Fe content increases up to 20 wt% on impregnation and decreases by a factor of ~2 on laser treatment of the 2 mmol/L-impregnated sample (see Fig S3). This indicates that a partial laser-induced dissolution / desorption of Fe cations on laser processing is neglectable for lower iron concentrations but becomes more pronounced above 1 mmol/L of the dopant precursor solution. Hereby it is likely that for higher concentrations either the monolayer adsorption of iron on the colloidal Co_3O_4 nanoparticles was exceeded or the electrochemical double layer around the respective colloidal nanoparticles was saturated with iron cations such that partial desorption or removal of excess iron occurred on laser processing in case of the high dopant concentrations. Which of the two possibilities applies here can however not be unequivocally discriminated against. Yet, the remaining iron concentration found by XPS and XRF after repeated laser processing undoubtedly shows that a substantial amount of Fe^{3+} was still present on the surface-near area of the laser-treated samples.

The XRD spectra of pulse series at low (0.5 mmol/L) and high (2 mmol/L) dopant concentrations show that no additional phases besides the initial Co_3O_4 were observed in Fig S4 and S5. Furthermore, the FeO(OH) clusters seen in the TEM (Fig 2 b) were not observed in XRD which indicates that they were either too small (signals too broad) to be detected or were present in amorphous form. Yet, interestingly, a slight but significant shift of the Co_3O_4 spinel signals towards smaller 2θ angles can be observed in Fig. S5 (b) and Fig. S6 (b) with an increasing number of employed laser pulses. This indicates an expansion of the unit cell which was further investigated by performing a Rietveld refinement of the XRD patterns.

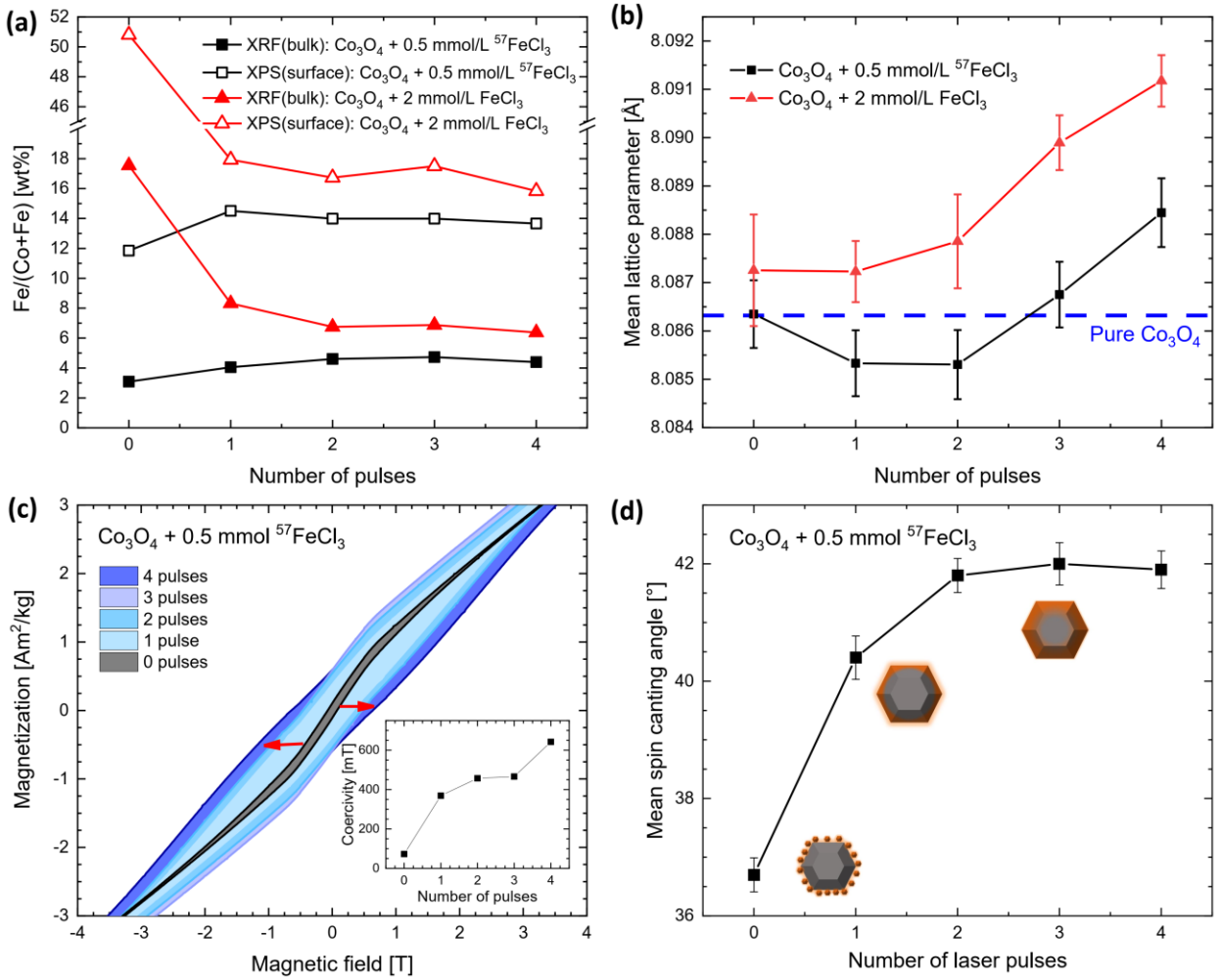

Figure 3: a) Iron content determined via XRF (bulk) and XPS (surface) from two sample series with an increasing number of applied laser pulses, prepared in a 2 mmol/L $FeCl_3$ and a 0.5 mmol/L $^{57}FeCl_3$ solution. B) The lattice parameter was determined from XRD-Rietveld refinement for the two sample series. c) Magnetization hysteresis from magnetometry measurements at 4.3 K of the ^{57}Fe enriched sample series, the inset shows the coercivity vs number of laser pulses (see Fig. S7 for full-field range). d) Mean spin canting angle determined from Mössbauer spectroscopy at 4.3 K and 5 T.

The lattice parameter of the samples within the laser pulse series of both high and low dopant concentration was determined by Rietveld refinement and is shown in Fig. 3 b. Particularly for the high dopant concentration, a gradual increase of the lattice parameter is found with an increasing number of single laser pulses considering the error bars determined from the fitting quality of the Rietveld refinement. In the case of a low dopant concentration, only pulse-by-pulse laser doping with more than two laser pulses indicates a slight increase. Considering that the lattice parameter of $CoFe_2O_4$ is ca. 8.38Å, an increase of the average lattice parameter from 8.086Å to 8.091 would indicate that when averaging over the whole particle volume, ~1-2 at% of Fe was doped into the Co_3O_4 lattice. Note, that this iron content resembles the iron that (i) potentially was incorporated

into the lattice and (ii) represents an average over the whole nanoparticle volume. In turn, the bulk-sensitive XRF results represent the sum of all iron (adsorbed on the Co_3O_4 surface and potentially laser-doped) and hence provide significantly higher iron contents. Finally, when comparing the size of the crystalline domains of pulse-by-pulse laser-doped samples (see Table S1) the domain size appears to remain unchanged at 38-39 nm for all samples. This confirms that no undesirable size change due to laser fragmentation or melting occurred during pulse-by-pulse laser processing of the iron precursor-impregnated colloidal Co_3O_4, respectively.

To further investigate potential laser-induced iron incorporation into the Co_3O_4 spinel structure, the samples that were laser-processed in the 0.5 mmol/L $^{57}FeCl_3$ precursor solution were investigated by magnetometry (Fig. 3 c, Fig. S7, and S8) and Mössbauer spectroscopy (see Fig. 2 d and Fig. S9 and S10). Magnetization curves recorded at 4.3 K display a gradually (linearly) increasing coercivity (compare inset Figure 3c) and remanence with the number of employed laser pulses. Note, that the increase of the magnetization hysteresis would also be expected in case of an increase in ^{57}Fe content, yet the XRF and XPS results in Fig 3 show a constant Fe content (within the range of ±1wt%) and an increasing number of pulse-by-pulse laser doping. Hence, the results in Fig. 3 indicate the presence of increasingly more uncompensated magnetic moments within the antiferromagnetic Co_3O_4 which points towards the incorporation of iron into the Co_3O_4 spinel after single and repeated laser-induced excitation.

To further probe the magnetic environment around the Fe^{3+}, Mössbauer spectra were recorded at 4.3 K as well as 5 T and display an asymmetric sextet structure (see Fig. S9) independent of laser treatment, which exhibits an average isomer shift of ca. 0.43 mm s^{-1} relative to α-Fe at room temperature. This observation can be attributed to Fe^{3+} states originating from the atom clusters at the particle surface that presumably represent the intermediary Fe^{3+}-reservoir. Regarding laser pulse driven Fe-transport, one can observe a clear increase in the relative line intensity ratio A_{23} being particularly prominent for the first laser pulse, which is indicative of the average spin alignment relative to the external magnetic field (Fig. S10). Average canting angles shown in Fig. 3 d are extracted from A_{23}.[36] The observed increase in spin frustration upon laser treatment supports the previous interpretation drawn from XRD that a fraction of Fe atoms were continuously incorporated into the antiferromagnetic Co_3O_4 material, where they don't display magnetic alignment, being consistent with results from magnetometry.

The previous XRD and Mössbauer results increasingly solidify that a successful gradual laser-induced pulse-by-pulse doping of the Co_3O_4 with the initially adsorbed Fe^{3+} precursor cations occurred. Yet, the question remains if the diffusion of Fe-ions into the Co_3O_4 lattice heated by an individual laser pulse with a pulse duration of ~7 ns is actually possible, considering that the timeframe where the particle temperature is sufficiently high to promote cation exchange and diffusion is limited to 10-20 ns. [37] Note that the diffusion coefficient, however, rises exponentially with the temperature.[38]

To estimate the possible diffusion depth initiated by a single laser pulse we used the common error function solution for Fick's second law to gain the time-dependent diffusion under consideration of the concentration gradient.[39] Hereby, the employed error function $\mathrm{erf}(y) = \frac{2}{\sqrt{\pi}} \int_0^y e^{-z^2} dz$ also considers interdiffusion:[40]

$$c(x,t) = \frac{c_s + c_b}{2} - \frac{c_s + c_b}{2} \mathrm{erf}\left(\frac{x}{2\sqrt{Dt}}\right) \quad (1)$$

We estimate the mole fraction of Fe on the surface to be $c_s = 1$ and in the bulk $c_b = 0$, therefore writing eq. 1 as:

$$c(x,t) = \frac{1 - \mathrm{erf}\left(\frac{x}{2\sqrt{Dt}}\right)}{2} \quad (2)$$

For calculation, we approximated the chemical diffusion coefficient of cation vacancies in Co_3O_4 ($D \approx 5 \cdot 10^{-8}$ cm^2 s^{-1}) determined at 1000 K by Grzesik et al.[41] The temperature is comparable to previous combined Mie- and Two-Temperature model calculations of the laser heating of Co_3O_4 with comparable laser intensity[27]. Following the study of Furlani et al. providing insight on the timeframe particles remain hot at different ns-pulse duration it is reasonable to expect that the particles remain hot for a duration of ~3 times the pulse duration[42] (in our case ~20 ns) per employed laser pulse. Based on this time frame, Fig. 4 shows an estimation of the Fe-concentration profiles initiated by laser-induced thermal cation diffusion.

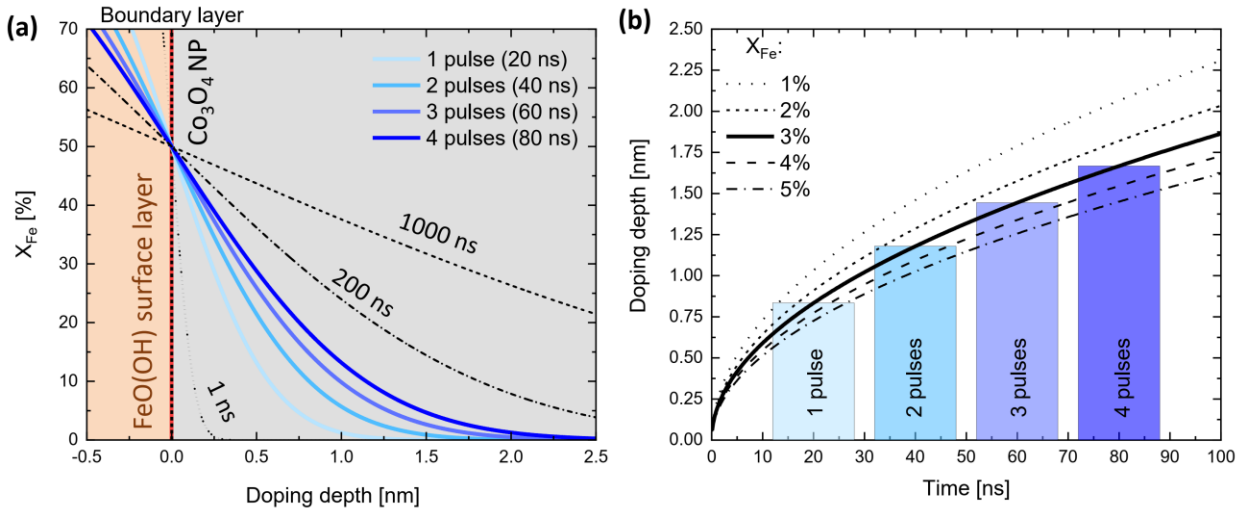

Figure 4: a) Calculated Fe-concentration profiles for the FeO(OH)/Co_3O_4 interface after ns-pulsed laser heating. b) Shows the calculated time-dependent doping depth for different threshold concentrations between 1-4%.

Note, that it appears unlikely that Fe^{3+} only occupies interstitial sites or cation vacancies. Hence, in this model, the iron concentration at the FeO(OH)/Co_3O_4 interface (*x=0*) was set to 50% (see Fig. 4 a) assuming doping mainly driven by an interdiffusion of iron into the Co_3O_4 lattice replacing cobalt ions that subsequently diffuse out of the Co_3O_4 and into the surrounding solution. The calculated diffusion depth shows a logarithmic increase with diffusion time and hence the number of laser pulses, respectively as can be seen in Fig. 4 b for different concentration thresholds. Therefore, the first applied laser pulse introduces the biggest doping depth of up to 0.75 nm which equals about 2 surface layers. Even though this estimation does not intend to provide exact predictions (considering the number of assumptions that had to be used) it yet shows that a laser-induced thermal diffusion of iron cations into the Co_3O_4 does occur on reasonable orders of magnitude to expect gradual pulse-by-pulse surface doping of the processed spinel catalysts. This further supports the interpretation of an increasing doping depth (and dopant concentration shown in XRD) with the rising number of laser pulses previously inferred from XRD (Fig. 3 b) and magnetometry studies (increase of the average spin canting angles as visible in Fig. 3 d). Furthermore, the coercivity shown in the inset in Fig. 3 c roughly follows a logarithmic increase as well, which is in very good agreement with the estimated thermally-induced diffusion-depth profiles in Fig 4 b.

To evaluate the effect of the iron doping with respect to the catalytic activity of the pulse-by-pulse laser-doped Co_3O_4 catalysts (in 2 mmol/L $FeCl_3$), their respective activity was investigated in two

different reactions, namely the gas-phase 2-propanol oxidation and the liquid-phase electrochemical oxygen evolution reaction. The 2-Propanol oxidation was performed via an in-situ-DRIFTS measurement (details are described in the SI below Fig. S11-S16). Fig. 5 a shows the normalized C-H peak areas determined by DRIFTS. Normalization of the C-H peak area was performed with respect to the peak area at 30°C where no conversion can be observed. From the activity profiles in Fig. 5 a, the $T_{50\%}$ value was determined as an activity-related coefficient representing the temperature where the initial C-H peak area (C-H bonds in 2-Propanol or of intermediates to CO_2) was reduced down to 50% (over a temperature ramp of 2 K min^{-1}). Subsequently, the respective activity parameter ($T_{50\%}$) of each investigated laser-doped sample was plotted against the previously estimated doping depth (see Fig. 5 b) for a gradually increasing number of pulse-by-pulse laser-doping steps (from solving Fick's second law and consideration of a projected effective laser-induced temperature at given laser intensity and heating time at given pulse duration, compare Fig. 4 b). Additionally, the activity of the same catalyst series was also determined for liquid phase OER from linear sweep voltammetry (LSV) shown in Fig. 5 c and summarized in Fig. 5 d by plotting the overpotential at 10 mA/cm^2 against the estimated, increasing doping depth.

Comparing both reaction profiles (gas-phase isopropanol oxidation and liquid-phase OER) in Fig. 5 b and d, respectively, the doped catalysts show a linear improvement of the catalytic activity with rising calculated dopant depth (proportional to the gradual increase of the number of applied laser pulses indicated as the upper x-axis in Fig. 5 b and d) in both reactions. In the case of the 2-Propanol oxidations, all Fe doped catalysts performed worse than the pure Co_3O_4 which is in agreement with the previous literature since particularly for non-laser treated iron impregnated Co_3O_4 the active site (fivefold coordinated Co_{5c}^{3+})[14] is being displaced by less active Fe^{3+}.[6] Since especially the first atomic layers strongly affects the catalytic activity, this observed gradual increase in catalytic activity with ongoing pulse-by-pulse doping (increasing number of laser pulses and expected doping depth) and the relater laser-induced interdiffusion of iron into the Co_3O_4 lattice potentially decreases the density of detrimental Fe^{3+} surface clusters on the catalyst surface. Respective conclusions are in strong agreement with the conclusion drawn from the increasing mean spin canting angle observed in Mössbauer spectroscopy (Fig. 3d). Yet, it stands to be noted that Mössbauer spectroscopy was performed with samples doped with low-concentrated (0.5 mmol/L) ^{57}Fe cations to be more sensitive to magnetic Fe-Co interactions while

the catalytic activity was analyzed for samples doped at a higher cation concentration of 2 mmol/L to ensure a sufficient sensitivity of this analysis to the presence of iron.

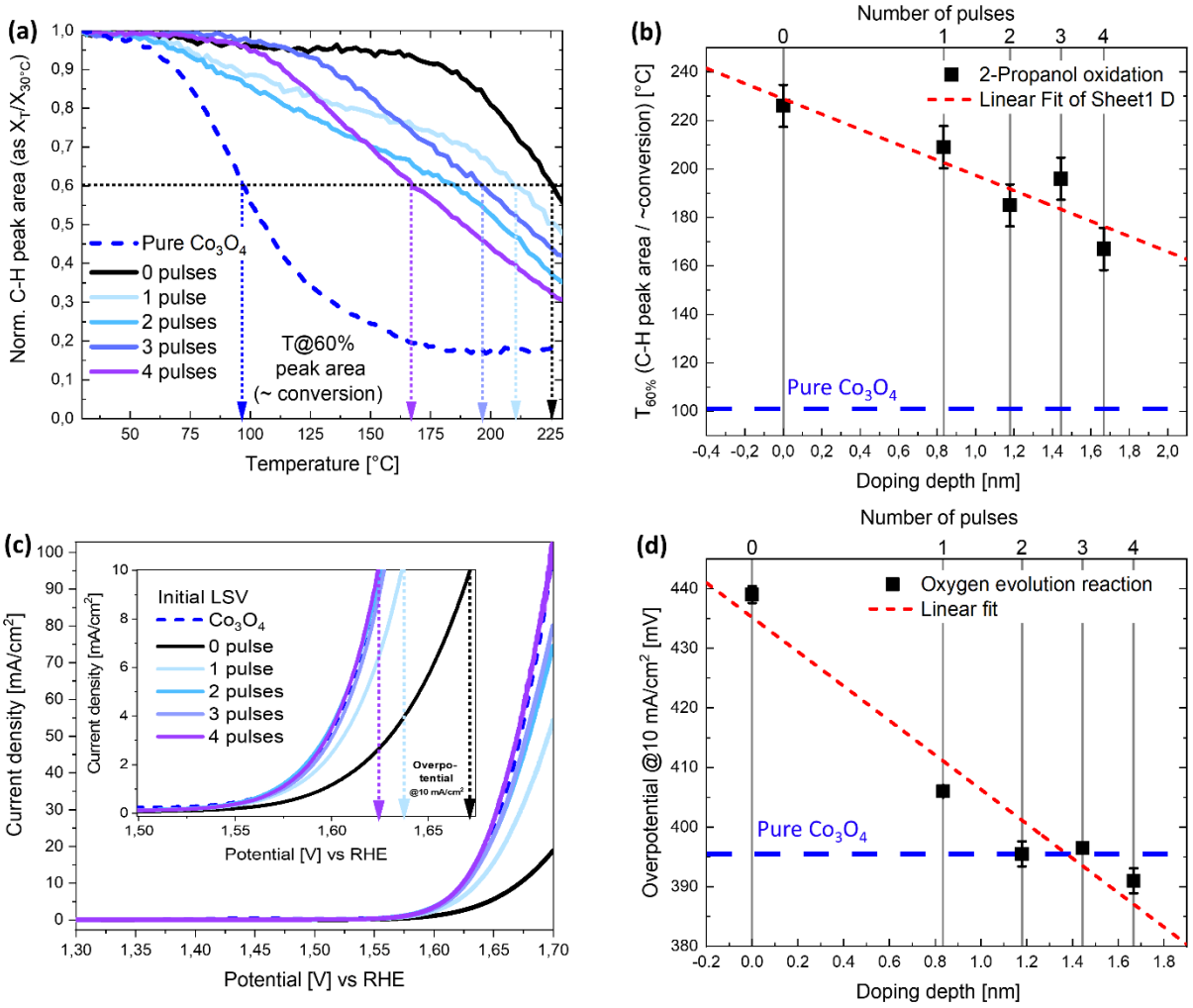

Figure 5 Comparison of the catalytic activity of nanoparticulate Co_3O_4 gradually laser-doped pulse-by-pulse in 2 mmol/L iron precursor concentration: (a) Temperature-dependent conversion of 2-propanol in gas-phase oxidation indicated by the normalized C-H peak area (to peak area at 30 °C representing the situation of negligible conversion) investigated by DRIFTS and (b) characteristic activity parameter for the selective 2-Propanol oxidation ($T_{50\%}$); (c) liquid-phase OER-activity, and (d) related overpotential @10mV for gradually increasing number of laser pulses proportional to the Fe cation doping depth.

In any case, the same trend is observed for the OER activity (Fig. 5 d), where the sample doped with 4 individual laser pulses and containing ~17 at% of Fe in the first 1-2 nm (XPS information depth[34]) even shows an exceeding activity compared to the initial Co_3O_4 that was completely untreated. These results are in line with Tüysüz et al., who observed an optimum activity at about 3 at% (Co:Fe ratio of 1:32) [5] of bulk iron-substituted Co_3O_4 spinel synthesized via the hard-templating method, while the sample containing ~13 at% Fe (Co:Fe ratio of 1:7)[5] was still slightly more active than pure Co_3O_4 in line with our results. They explain this increase in activity with an

increasing ratio of Co^{2+} on the tetrahedral sites compared to Co^{3+} on the octahedral sites, where the tetrahedral ones were proposed as an active site for the formation of μ-OOH moieties in the intermediate state of OER[43]. The tetrahedral to octahedral occupation ratio increase might occur due to the displacement of Co on the octahedral sites by Fe, which at a low amount, could also enhance the conductivity of the cobalt-iron oxyhydroxide intermediate active state during the applied potential bias.[44] In our case, the impregnated but non-laser processed sample (0 pulses) shows a strongly inhibited activity compared to the pristine Co_3O_4 most likely due to the formation of insulating iron (oxy)hydroxide layer/clusters[32,33] after adsorption of the iron precursor on impregnation which resembles a very high iron concentration in the catalytically-relevant first outer surface layer. This insulating layer hampers the charge transfer and is detrimental to overall OER activity. With the increasing number of laser pulses, similar to the results in 2-propanol oxidation the OER activity of the samples also increases due to the incorporation of iron into the spinel surface and diminishing the insulating iron (oxy)hydroxide clusters.

Considering the catalytic stability, the sample treated with 4 pulses is less prone to deactivation when comparing the initial activity during the 1st and the 50th cycle (see Fig. S17 c and d). In turn, the impregnated samples where no laser pulses were applied (0 Pulses; see Fig. S17 b and d) show a particular deactivation after 50 voltammetry cycles. The deactivation might be correlated to the existence of iron (oxy)hydroxide clusters on the surface of the catalyst, that is prone to be deactivated in a harsh alkaline environment due to the leaching or oxidation into a soluble FeO_4^{2-} at a high anodic potential as suggested by the Pourbaix diagram.[44–47] This increasing resistance to the deactivation on 4 laser pulses further solidifies that the laser processing successfully induces the incorporation of iron into the spinel surface and creates a stable iron-doped spinel phase.

4 Conclusion

In this study, we investigated the pulse-by-pulse laser doping of aqueous iron salt precursor-impregnated colloidal Co_3O_4 nanoparticles under repeated single laser pulse excitation using a flat liquid jet setup and uniform irradiation conditions. Before the first laser pulse was applied, HR-TEM showed that the iron cations from the $FeCl_3$ precursor solution adsorbed onto the Co_3O_4 surface, forming small clusters (1-3 nm) of iron oxyhydroxide after sample preparation (drying) and subsequent washing. These surface clusters were shown to disappear upon laser treatment of

the impregnated colloidal Co_3O_4 nanoparticles with the first single laser pulse causing the formation of disordered surface layers. Such disordered layers were recently reported to form after laser-based defect-writing of colloidal $CoFe_2O_4$ nanoparticles.[29] XRF as bulk-sensitive quantification method shows a constant iron concentration of ~ 9 wt% in the laser-doped catalysts over several individual laser pulses. Accordingly, XPS resembling a surface-sensitive method shows the same trends as XRF but with more than 2x the iron content since the iron is concentrated on the surface. XRD indicates a steady increase of the lattice parameter with laser processing and dopant concentration indicating the incorporation of iron throughout the sequentially pulsed laser doping. A comparison to the lattice parameter of the laser-doped samples with $CoFe_2O_4$ and Fe_3O_4 is in agreement with an average of 1-2at% embedded Fe. Magnetometry measurements of impregnated but non-laser processed Co_3O_4 showed the characteristic antiferromagnetic behavior of spinel Co_3O_4 with barely any hysteresis and low coercivity. After individual laser pulses were employed pulse-by-pulse to the impregnated colloidal Co_3O_4, the hysteresis and coercivity gradually increases with the number of laser pulses exhibiting the largest increase after the 1st laser pulse. The same trend is observed from Mössbauer spectroscopy showing a logarithmic increase of the mean spin canting angle with a rising number of subsequently employed laser pulses. Both observations show that an increasing interaction of the Fe cations with the antiferromagnetic Co_3O_4 support occurred after individual laser pulses were employed, supporting in line with XRD that a successful laser-induced cation doping occurred. Since nanosecond laser pulses were employed throughout the doping process only very short heating and hence diffusion duration~~s~~ of several 10^{th} of ns had to be expected. To evaluate, if a thermally-induced diffusion of the iron cation into a laser-heated Co_3O_4 initiated by an individual laser pulse (here 7 ns pulse duration) represents a realistic scenario for pulse-by-pulse laser doping of colloidal nanoparticles, the order of magnitude of the diffusion depth after laser excitation was estimated by solving Fick's 2^{nd} law at previously calculated laser-induced temperature (of 800 – 1000 °C)[27] related diffusion constants[41] and expected duration where the particle is hot (~20 ns per laser pulse at given pulse duration[42]). The results suggest that at a depth of 1 nm a mole fraction of 1% Fe is reached after the first laser pulse and after the fourth laser pulse iron is expected to have diffused roughly 2 nm into the Co_3O_4 nanoparticle surface. Further, a logarithmic increase of the doping depth with an increasing number of applied laser pulses was found which is in good agreement with the trends observed for the coercivity and spin canting angle determined from magnetometry and Mössbauer

spectroscopy, respectively solidifying a successful laser cation doping of colloidal nanoparticles. To evaluate the applicability of a gradual laser pulse-by-pulse iron-doped Co_3O_4 catalyst series in catalytic studies the material series was finally tested regarding their activity in gas-phase isopropanol oxidation and liquid-phase OER. The observed catalytic activity trends of the laser-doped catalysts were in good agreement with previously published composition series gained from different impregnation techniques to synthesize a nanoparticulate Fe:Co catalysts composition series demonstrating comparability of the developed gradual laser-doping of cations to conventional synthesis methods.[5–7] Reusability tests further showed good catalytic stability of the catalysts after the first, as well as subsequent laser pulses, were employed while non-laser processed catalysts deactivated in OER most-likely due to leaching and detrimental oxidation processes. For both reactions, the catalytic activity of the pulse-by-pulse laser-doped iron-impregnated Co_3O_4 catalysts was found to gradually increase with the rising number of employed individual laser pulses. When referencing the catalytic activity of the sample series with the expected thermally-induced doping depth, a linear improvement of the catalytic activity was overserved for both reaction types highlighting an imminent strength of laser-doping in providing gradual catalyst doping series to study and identify composition related active sites and reaction mechanisms in future catalytic studies. Overall, this paper demonstrates the feasibility of pulse-by-pulse laser surface cation doping of colloidal nanoparticles to provide comparable, active, and stable catalyst series to investigate composition-dependent catalytic activity profiles and identify active sites and reaction mechanisms in future catalytic studies.

Acknowledgements

We gratefully acknowledge the DFG Deutsche Forschungsgemeinschaft for its financial support under Project 388390466 - TRR 247. Dr. Marcus Heidelmann (ICAN) and Jurji Jacobi are acknowledged for assistance with HR-TEM measurements. HT thanks Max Planck Society for the basic funding.

5 References

(1) *Metal oxides*:*Chemistry and applications*; Taylor & Francis, 2006.

(2) Parravano, G. The Catalytic Oxidation of Carbon Monoxide on Nickel Oxide. II. Nickel Oxide Containing Foreign Ions. *Journal of the American Chemical Society* **1953**, *75* (6), 1452–1454. DOI: 10.1021/ja01102a051.

(3) McFarland, E. W.; Metiu, H. Catalysis by doped oxides. *Chemical reviews* **2013**, *113* (6), 4391–4427. DOI: 10.1021/cr300418s. Published Online: Jan. 27, 2013.

(4) Anke, S.; Falk, T.; Bendt, G.; Sinev, I.; Hävecker, M.; Antoni, H.; Zegkinoglou, I.; Jeon, H.; Knop-Gericke, A.; Schlögl, R.; Roldan Cuenya, B.; Schulz, S.; Muhler, M. On the reversible deactivation of cobalt ferrite spinel nanoparticles applied in selective 2-propanol oxidation. *Journal of Catalysis* **2020**, *382*, 57–68. DOI: 10.1016/j.jcat.2019.12.007.

(5) Budiyanto, E.; Yu, M.; Chen, M.; DeBeer, S.; Rüdiger, O.; Tüysüz, H. Tailoring Morphology and Electronic Structure of Cobalt Iron Oxide Nanowires for Electrochemical Oxygen Evolution Reaction. *ACS Appl. Energy Mater.* **2020**, *3* (9), 8583–8594. DOI: 10.1021/acsaem.0c01201.

(6) Waffel, D.; Budiyanto, E.; Porske, T.; Büker, J.; Falk, T.; Fu, Q.; Schmidt, S.; Tüysüz, H.; Muhler, M.; Peng, B. Investigation of Synergistic Effects between Co and Fe in Co3-xFexO4 Spinel Catalysts for the Liquid-Phase Oxidation of Aromatic Alcohols and Styrene. *Molecular Catalysis* **2020**, *498*, 111251. DOI: 10.1016/j.mcat.2020.111251.

(7) Falk, T.; Budiyanto, E.; Dreyer, M.; Pflieger, C.; Waffel, D.; Büker, J.; Weidenthaler, C.; Ortega, K. F.; Behrens, M.; Tüysüz, H.; Muhler, M.; Peng, B. Identification of Active Sites in the Catalytic Oxidation of 2-Propanol over Co 1+x Fe 2–x O 4 Spinel Oxides at Solid/Liquid and Solid/Gas Interfaces. *ChemCatChem* **2021**, *13* (12), 2942–2951. DOI: 10.1002/cctc.202100352.

(8) Waag, F.; Gökce, B.; Kalapu, C.; Bendt, G.; Salamon, S.; Landers, J.; Hagemann, U.; Heidelmann, M.; Schulz, S.; Wende, H.; Hartmann, N.; Behrens, M.; Barcikowski, S. Adjusting the catalytic properties of cobalt ferrite nanoparticles by pulsed laser fragmentation in water with defined energy dose. *Scientific reports* **2017**, *7* (1), 13161. DOI: 10.1038/s41598-017-13333-z.

(9) Yu, M.; Waag, F.; Chan, C. K.; Weidenthaler, C.; Barcikowski, S.; Tüysüz, H. Laser fragmentation induced defect-rich cobalt oxide nanoparticles for electrochemical oxygen evolution reaction. *ChemSusChem* **2019.** DOI: 10.1002/cssc.201903186.

(10) Saddeler, S.; Hagemann, U.; Schulz, S. Effect of the Size and Shape on the Electrocatalytic Activity of Co3O4 Nanoparticles in the Oxygen Evolution Reaction. *Inorg. Chem.* **2020**, *59* (14), 10013–10024. DOI: 10.1021/acs.inorgchem.0c01180. Published Online: Jun. 26, 2020.

(11) Chakrapani, K.; Bendt, G.; Hajiyani, H.; Schwarzrock, I.; Lunkenbein, T.; Salamon, S.; Landers, J.; Wende, H.; Schlögl, R.; Pentcheva, R.; Behrens, M.; Schulz, S. Role of Composition and Size of Cobalt Ferrite Nanocrystals in the Oxygen Evolution Reaction. *ChemCatChem* **2017**, *9* (15), 2988–2995. DOI: 10.1002/cctc.201700376.

(12) Quast, T.; Varhade, S.; Saddeler, S.; Chen, Y.-T.; Andronescu, C.; Schulz, S.; Schuhmann, W. Single Particle Nanoelectrochemistry Reveals the Catalytic Oxygen Evolution Reaction Activity of Co3O4 Nanocubes. *Angewandte Chemie (International ed. in English)* **2021.** DOI: 10.1002/anie.202109201. Published Online: Aug. 19, 2021.

(13) El Arrassi, A.; Liu, Z.; Evers, M. V.; Blanc, N.; Bendt, G.; Saddeler, S.; Tetzlaff, D.; Pohl, D.; Damm, C.; Schulz, S.; Tschulik, K. Intrinsic Activity of Oxygen Evolution Catalysts Probed at Single CoFe2O4 Nanoparticles. *Journal of the American Chemical Society* **2019**, *141* (23), 9197–9201. DOI: 10.1021/jacs.9b04516. Published Online: Jun. 3, 2019.

(14) Anke, S.; Bendt, G.; Sinev, I.; Hajiyani, H.; Antoni, H.; Zegkinoglou, I.; Jeon, H.; Pentcheva, R.; Roldan Cuenya, B.; Schulz, S.; Muhler, M. Selective 2-Propanol Oxidation over Unsupported Co 3 O 4 Spinel Nanoparticles: Mechanistic Insights into Aerobic Oxidation of Alcohols. *ACS Catal.* **2019**, *9* (7), 5974–5985. DOI: 10.1021/acscatal.9b01048.

(15) Krstulović, N.; Salamon, K.; Budimlija, O.; Kovač, J.; Dasović, J.; Umek, P.; Capan, I. Parameters optimization for synthesis of Al-doped ZnO nanoparticles by laser ablation in water. *Applied Surface Science* **2018**, *440*, 916–925. DOI: 10.1016/j.apsusc.2018.01.295.

(16) Ludwig, A. Discovery of new materials using combinatorial synthesis and high-throughput characterization of thin-film materials libraries combined with computational methods. *npj Comput Mater* **2019**, *5* (1). DOI: 10.1038/s41524-019-0205-0.

(17) Zolper, J. C.; Wilson, R. G.; Pearton, S. J.; Stall, R. A. Ca and O ion implantation doping of GaN. *Appl. Phys. Lett.* **1996**, *68* (14), 1945–1947. DOI: 10.1063/1.115634.

(18) Hallam, B.; Chan, C.; Sugianto, A.; Wenham, S. Deep junction laser doping for contacting buried layers in silicon solar cells. *Solar Energy Materials and Solar Cells* **2013**, *113*, 124–134. DOI: 10.1016/j.solmat.2013.02.011.

(19) Amendola, V.; Amans, D.; Ishikawa, Y.; Koshizaki, N.; Scirè, S.; Compagnini, G.; Reichenberger, S.; Barcikowski, S. Room-Temperature Laser Synthesis in Liquid of Oxide, Metal-Oxide Core-Shells, and Doped Oxide Nanoparticles. *Chemistry (Weinheim an der Bergstrasse, Germany)* **2020.** DOI: 10.1002/chem.202000686.

(20) Dalpian, G. M.; Chelikowsky, J. R. Self-purification in semiconductor nanocrystals. *Phys. Rev. Lett.* **2006**, *96* (22), 226802. DOI: 10.1103/physrevlett.96.226802. Published Online: Jun. 6, 2006.

(21) Carey, P. G.; Sigmon, T. W. In-situ doping of silicon using the gas immersion laser doping (GILD) process. *Applied Surface Science* **1989**, *43* (1-4), 325–332. DOI: 10.1016/0169-4332(89)90234-1.

(22) Bet, S.; Quick, N.; Kar, A. Effect of laser field and thermal stress on diffusion in laser doping of SiC. *Acta Materialia* **2007**, *55* (20), 6816–6824. DOI: 10.1016/j.actamat.2007.08.039.

(23) Lin, Z.; Du, C.; Yan, B.; Wang, C.; Yang, G. Two-dimensional amorphous NiO as a plasmonic photocatalyst for solar H2 evolution. *Nature Communications* **2018**, *9* (1), 4036. DOI: 10.1038/s41467-018-06456-y.

(24) Liang, S.-X.; Salamon, S.; Zerebecki, S.; Zhang, L.-C.; Jia, Z.; Wende, H.; Reichenberger, S.; Barcikowski, S. A laser-based synthesis route for magnetic metallic glass nanoparticles. *Scripta Materialia* **2021**, *203*, 114094. DOI: 10.1016/j.scriptamat.2021.114094.

(25) Liang, S.-X.; Zhang, L.-C.; Reichenberger, S.; Barcikowski, S. Design and perspective of amorphous metal nanoparticles from laser synthesis and processing. *Physical chemistry chemical physics : PCCP* **2021**, *23* (19), 11121–11154. DOI: 10.1039/d1cp00701g. Published Online: May. 10, 2021.

(26) Peng, Y.; Cao, J.; Sha, Y.; Yang, W.; Li, L.; Liu, Z. Laser solid-phase synthesis of single-atom catalysts. *Light, science & applications* **2021**, *10* (1), 168. DOI: 10.1038/s41377-021-00603-9. Published Online: Aug. 18, 2021.

(27) Budiyanto, E.; Zerebecki, S.; Weidenthaler, C.; Kox, T.; Kenmoe, S.; Spohr, E.; DeBeer, S.; Rüdiger, O.; Reichenberger, S.; Barcikowski, S.; Tüysüz, H. Impact of Single-Pulse, Low-Intensity Laser Post-Processing on Structure and Activity of Mesostructured Cobalt Oxide for the Oxygen Evolution Reaction. *ACS Appl. Mater. Interfaces* **2021.** DOI: 10.1021/acsami.1c08034. Published Online: Jul. 29, 2021.

(28) Zerebecki, S.; Reichenberger, S.; Barcikowski, S. Continuous-Flow Flat Jet Setup for Uniform Pulsed Laser Postprocessing of Colloids. *The journal of physical chemistry. A* **2020**, *124* (52), 11125–11132. DOI: 10.1021/acs.jpca.0c08787. Published Online: Dec. 16, 2020.

(29) Zerebecki, S.; Salamon, S.; Landers, J.; Yang, Y.; Tong, Y.; Budiyanto, E.; Waffel, D.; Dreyer, M.; Saddeler, S.; Kox, T.; Kenmoe, S.; Spohr, E.; Schulz, S.; Behrens, M.; Muhler, M.; Tüysüz, H.; Campen, R. K.; Wende, H.; Reichenberger, S.; Barcikowski, S. Engineering of Cation Occupancy of CoFe2O4 Oxidation Catalysts by Nanosecond, Single-Pulse Laser Excitation in Water. *(Accepted).*

(30) Oriekhova, O.; Stoll, S. Investigation of FeCl3 induced coagulation processes using electrophoretic measurement, nanoparticle tracking analysis and dynamic light scattering: Importance of pH and colloid surface charge. *Colloids and Surfaces A: Physicochemical and Engineering Aspects* **2014**, *461*, 212–219. DOI: 10.1016/j.colsurfa.2014.07.049.

(31) https://www.uni-due.de/~hm236ap/hoersten/home.html.

(32) Gilbert, B.; Lu, G.; Kim, C. S. Stable cluster formation in aqueous suspensions of iron oxyhydroxide nanoparticles. *Journal of colloid and interface science* **2007**, *313* (1), 152–159. DOI: 10.1016/j.jcis.2007.04.038. Published Online: Apr. 20, 2007.

(33) Fu, D.; Keech, P. G.; Sun, X.; Wren, J. C. Iron oxyhydroxide nanoparticles formed by forced hydrolysis: dependence of phase composition on solution concentration. *Physical chemistry chemical physics : PCCP* **2011**, *13* (41), 18523–18529. DOI: 10.1039/c1cp20188c. Published Online: Sep. 22, 2011.

(34) Vaz, C. A. F.; Prabhakaran, D.; Altman, E. I.; Henrich, V. E. Experimental study of the interfacial cobalt oxide in Co3O4/α−Al2O3(0001) epitaxial films. *Phys. Rev. B* **2009**, *80* (15). DOI: 10.1103/PhysRevB.80.155457.

(35) Kaufmann, M.; Mantler, M.; Weber, F. Analysis of Multi-Layer Thin Films by XRF. *Adv. x-ray anal.* **1993**, *37*, 205–212. DOI: 10.1154/S0376030800015706.

(36) Landers, J.; Salamon, S.; Webers, S.; Wende, H. Microscopic understanding of particle-matrix interaction in magnetic hybrid materials by element-specific spectroscopy. *Physical Sciences Reviews* **2021**, *0* (0). DOI: 10.1515/psr-2019-0116.

(37) Ziefuss, A. R.; Reich, S.; Reichenberger, S.; Levantino, M.; Plech, A. In situ structural kinetics of picosecond laser-induced heating and fragmentation of colloidal gold spheres. *Physical chemistry chemical physics : PCCP* **2020**, *22* (9), 4993–5001. DOI: 10.1039/c9cp05202j.

(38) JOST, W. Diffusion in Solids. *Liquid, Gases* **1960**, *73*.

(39) Cussler, E. L. *Diffusion*:*Mass transfer in fluid systems*, 2. ed., reprint; Cambridge series in chemical engineering; Cambridge Univ. Press, 2000.

(40) Jacobs, M. H. *Diffusion Processes*; Springer, 1967.

(41) Grzesik, Z.; Kaczmarska, A.; Mrowec, S. Nonstoichiometry and Chemical Diffusion in Co_3O_4 Cobalt Oxide. *SSP* **2015**, *227*, 421–424. DOI: 10.4028/www.scientific.net/SSP.227.421.

(42) Furlani, E. P.; Karampelas, I. H.; Xie, Q. Analysis of pulsed laser plasmon-assisted photothermal heating and bubble generation at the nanoscale. *Lab on a chip* **2012**, *12* (19), 3707–3719. DOI: 10.1039/c2lc40495h.

(43) Hsu, S.-H.; Hung, S.-F.; Wang, H.-Y.; Xiao, F.-X.; Zhang, L.; Yang, H.; Chen, H. M.; Lee, J.-M.; Liu, B. Tuning the Electronic Spin State of Catalysts by Strain Control for Highly Efficient Water Electrolysis. *Small Methods* **2018**, *2* (5), 1800001. DOI: 10.1002/smtd.201800001.

(44) Burke, M. S.; Kast, M. G.; Trotochaud, L.; Smith, A. M.; Boettcher, S. W. Cobalt-iron (oxy)hydroxide oxygen evolution electrocatalysts: the role of structure and composition on activity, stability, and mechanism. *Journal of the American Chemical Society* **2015**, *137* (10), 3638–3648. DOI: 10.1021/jacs.5b00281. Published Online: Mar. 4, 2015.

(45) Luo, W.; Jiang, C.; Li, Y.; Shevlin, S. A.; Han, X.; Qiu, K.; Cheng, Y.; Guo, Z.; Huang, W.; Tang, J. Highly crystallized α-FeOOH for a stable and efficient oxygen evolution reaction. *J. Mater. Chem. A* **2017**, *5* (5), 2021–2028. DOI: 10.1039/C6TA08719A.

(46) Zou, S.; Burke, M. S.; Kast, M. G.; Fan, J.; Danilovic, N.; Boettcher, S. W. Fe (Oxy)hydroxide Oxygen Evolution Reaction Electrocatalysis: Intrinsic Activity and the Roles of Electrical Conductivity, Substrate, and Dissolution. *Chem. Mater.* **2015**, *27* (23), 8011–8020. DOI: 10.1021/acs.chemmater.5b03404.

(47) Beverskog, B.; Puigdomenech, I. Revised pourbaix diagrams for iron at 25–300 °C. *Corrosion Science* **1996**, *38* (12), 2121–2135. DOI: 10.1016/S0010-938X(96)00067-4.